Tuneable Piezoresistance of Graphene-Based 2D:2D Nanocomposite Networks

*James R. Garcia, Mark McCrystal, Dominik Horváth, Harneet Kaur, Tian Carey, and Jonathan N. Coleman**

Piezoresistive nanocomposites are an important class of materials that allow the production of very sensitive strain sensors. Herein, a new class of piezoresistive nanocomposites prepared by mixing different types of 2D nanosheets is explored. In this way, three distinct types of nanocomposite are produced by mixing conducting and insulating nanosheets (graphene, Gr and boron nitride, BN), conducting and semi-conducting nanosheets (graphene and tungsten diselenide, WSe_2 or tungsten disulfide, WS_2) as well as mixing two different types of conducting nanosheets (graphene and silver, Ag). For each nanocomposite type, a different dependence of composite conductivity on filler volume fraction is observed although all behaviors can be fully described by percolation theory. In addition, each composite type shows different piezoresistive properties. Interestingly, while the conductor insulator composites show the standard monotonic relationship between gauge factor and conductivity, both conductor:semi-conductor and conductor:conductor composites show very unusual behavior, in each case displaying a peak engage factor at the percolation threshold. In each case, percolation theory is used to develop simple equations for gauge factor as a function of both volume fraction and conductivity that fully describes all experimental data. This work expands the understanding of piezoresistive nanocomposites and provides a platform for the engineering of high-performance strain sensors.

1. Introduction

The evolution of the Internet of Things has generated much interest in the development of ubiquitous sensing platforms. However, to realise such new technologies, sensors that are highly accurate and cost effective will be required, detecting a range of parameters, including temperature, presence of chemicals, and strain.[1,2] Here, nanomaterials have shown great promise, due to their low cost, high versatility, and the ease with which they can be processed into functional devices.[3–5]

Of particular interest are electromechanical sensors, where the applied stress, pressure or strain associated with mechanical deformation is detected via a change in the electrical properties of the sensor, typically in the form of a change in resistance. The sensitivity of such piezoresistive sensors is described by a figure of merit known as the gauge factor (G), which describes the relative resistance change of the sensor, $\Delta R/R_0 = G\varepsilon$, where ΔR is the change in resistance, R_0 is the zero-strain resistance, and ε is the applied strain. In order to realise industry compatible sensing devices, $\Delta R/R_0$ should vary linearly with applied strain such that G has a well-defined single value, a condition that usually applies at low strain. Metal foil strain gauges are standard in industry, owing to the fact that they are cheap, effective, and easy to produce. However, these sensors have a significant drawback, namely, that their gauge factors are low ($G \approx 2$ within a 0–3% strain range).[6]

Nanostructured piezoresistive strain sensors are a class of materials whose sensitivities have been shown to far surpass their metal foil counterparts. In addition, they are easy to fabricate[7] and can be very soft,[8] making them suitable for wearable applications. These materials can detect minute deformations that have made them highly effective in the area of vital sign and health monitoring where tiny fluctuations in skin position must be detected.[9,10] Nanostructured piezoresistive strain sensors typically come in two forms: conductive nanomaterials embedded into polymer matrices as nanocomposites[10] and conductive nanomaterials fabricated into thin films on polymer substrates.[11]

Polymer nanocomposites have attracted attention due to their versatility that enables tuneable gauge factors by simply changing the concentration of filler within the polymer matrix.[8,12,13] However, the conductivity in such systems can be low due to the ubiquitous polymer coating that surrounds the conductive filler thus limiting efficient charge transfer.[14]

J. R. Garcia, M. McCrystal, D. Horváth, H. Kaur, T. Carey, J. N. Coleman
School of Physics, CRANN & AMBER Research Centres
Trinity College Dublin
D02 PN40 Dublin, Ireland
E-mail: colemaj@tcd.ie

**ADVANCED
SCIENCE NEWS**

www.advancedsciencenews.com

**ADVANCED
FUNCTIONAL
MATERIALS**

www.afm-journal.de

The mechanical properties of the polymer matrix are also highly dependent on filler content, and while increasing the concentration of conductive particles increases the overall conductivity of the nanocomposite,[15] it often leads to stiffer and more brittle materials.[16] In terms of their sensing performance polymer nanocomposites can display large electrical hysteresis[17,18] as well as strain rate[19,20] and frequency[7] dependent effects that further complicate facile sensor fabrication.

Thin nanomaterial films supported by polymer substrates offer an attractive alternative since the mechanical properties of the sensor depend on the mechanics of the substrate, while the electrical and piezoresistive properties are determined by the particle network.[7,21] A variety of thin film nanostructured sensors have been reported based on printed networks,[22] thin films fabricated on pre-strained substrates,[23] cracked networks,[24] and various combinations of 0D, 1D, and 2D conductors.[25–31] Such sensors have demonstrated very high sensitivity (G up to ≈350) as well as good cyclability, low hysteresis, and frequency independence.[22] However, the mechanisms behind sensor performance are poorly understood, which has led to there having little control over sensor conductivity or sensitivity.

At present, the only reliable control of sensitivity and conductivity in nanostructured thin film strain sensors, comes from single nanomaterial networks, where sensitivity can be tuned by controlling film thickness.[22,32,33] Thus, it would be useful if other methods could be exploited to control the piezoresistive response, opening the door to novel types of sensor design as well as giving some insight into the mechanisms underlying piezo-resistive networks. We propose that combining different nanomaterials to form thin film nano:nano composites is a promising strategy to yield printable, high-performance piezoresistive materials with tuneable sensitivity. Nano:nano composites are distinct from polymer nanocomposites or single nanomaterial networks since the interaction between the nanomaterial components can have a dramatic effect on both the electrical and piezoresistive properties.[25–27,30–31,34–36] For example, CNTs have been used to dramatically increase the sensing range of 2D networks,[25–27] while MoS2:Graphene networks display minimal electrical hysteresis (≈2.75%).[35] These reports demonstrate that by mixing appropriate nanomaterials, improved sensor designs can be readily achieved.

Here, we present novel 2D:2D nano:nano composites as thin film strain sensors. These comprise two-phase mixtures of conducting, semiconducting, and insulating 2D materials. We show that sensor performance is intimately linked to both composition and percolative parameters of each nanocomposite, offering unique tunability of gauge factor alongside sensor conductivity. We furthermore develop a general model for percolative nanocomposite systems, which can guide future progress toward high-performance strain sensors.

2. Results and Discussion

2.1. Materials and Characterization

Here, we will study the piezoresistive properties of nano:nano composite[37] thin films prepared from mixtures of various types of conducting (silver and graphene nanosheets), semiconducting (WSe_2 and WS_2 nanosheets), and insulating (BN nanosheets) 2D materials. The first step toward film formation is to prepare inks of each material. Inks of Graphene (Gr), WSe_2, WS_2, and BN nanosheets were produced by liquid phase exfoliation (LPE, see Experimental Section), which has been shown as an effective method for producing few layer nanosheets.[38,39] Highly concentrated water-based pastes of silver nanosheets (AgNS) are commercially available[40] with workable inks achievable via simple dilution.

A photograph of the resultant inks is shown in **Figure 1**A. Optical extinction spectra of each dispersion are presented in Figure 1B, with each spectrum showing the appropriate features. The characteristic high frequency plateau and π–π^* peak are observed for graphene,[41] while BN displays the expected broad scattering background.[42] Both WS_2 and WSe_2 display their main spectral features, namely A excitons at 640 nm[43,44] for WS_2 and 755 nm[44] for WSe_2. The AgNS spectra contain features at 350 and 400 nm, respectively, which are typically observed in spectra of silver nano-plates,[45] -bars,[46] -particles,[47] and -wires[48] and have previously been attributed to surface plasmon resonances (although the exact location of the features depends on the dimensionality of the silver). Transmission Electron Microscopy (TEM) (Figure 1C,D) confirms the presence of nanosheets in all prepared dispersions with no non-2D materials observed. Nanosheet length statistics can be extracted from TEM images, as demonstrated in Figure 1D (see Supporting Information for histograms of other materials). The average nanosheet length (defined as the longest nanosheet axis) for each nanosheet ink, $<L_{Gr}>$ = 348, $<L_{BN}>$ = 327, $<L_{Ag}>$ = 251, $<L_{WSe_2}>$ = 161, and $<L_{WS_2}>$ = 197 nm was found from a minimum of 110 counts. Raman spectra, measured on drop cast-films (Figure 1E,F), showed all the expected features consistent with literature reports on 2D nanosheets of graphene,[41] WS_2,[49] WSe_2,[49] and BN.[42]

The individual inks were mixed to produce nano:nano composite inks with the following compositions: BN:Gr, WSe_2:Gr, WS_2:Gr, Ag:Gr. For each composition, various mixtures were made leading to a range of mass-fractions of each component. The composite inks were used to produce thin nano:nano composite films by spray coating onto polyimide substrates. An example of such a film is shown in Figure 1G. The spray-coated films had a thickness between 600 and 1000 nm and should therefore be free of any thickness dependent effects.[22,40,50,51]

2.2. Network Morphology

Scanning electron microscope images (**Figure 2**A–D) of the prepared composite films show disordered and porous networks. The films appear uniform over large length scales with graphene nanosheets (dark) mixed reasonably well with BN, WSe_2, WS_2, and Ag (lighter) nanosheets (See Supporting Information for EDX maps). Polymer-based nanocomposites are usually described via a filler (the nanomaterial) and a matrix (the polymer). In order to properly analyze the electrical properties of nanocomposites, it is necessary to convert the filler mass fraction, M_f, to volume fraction. In general,
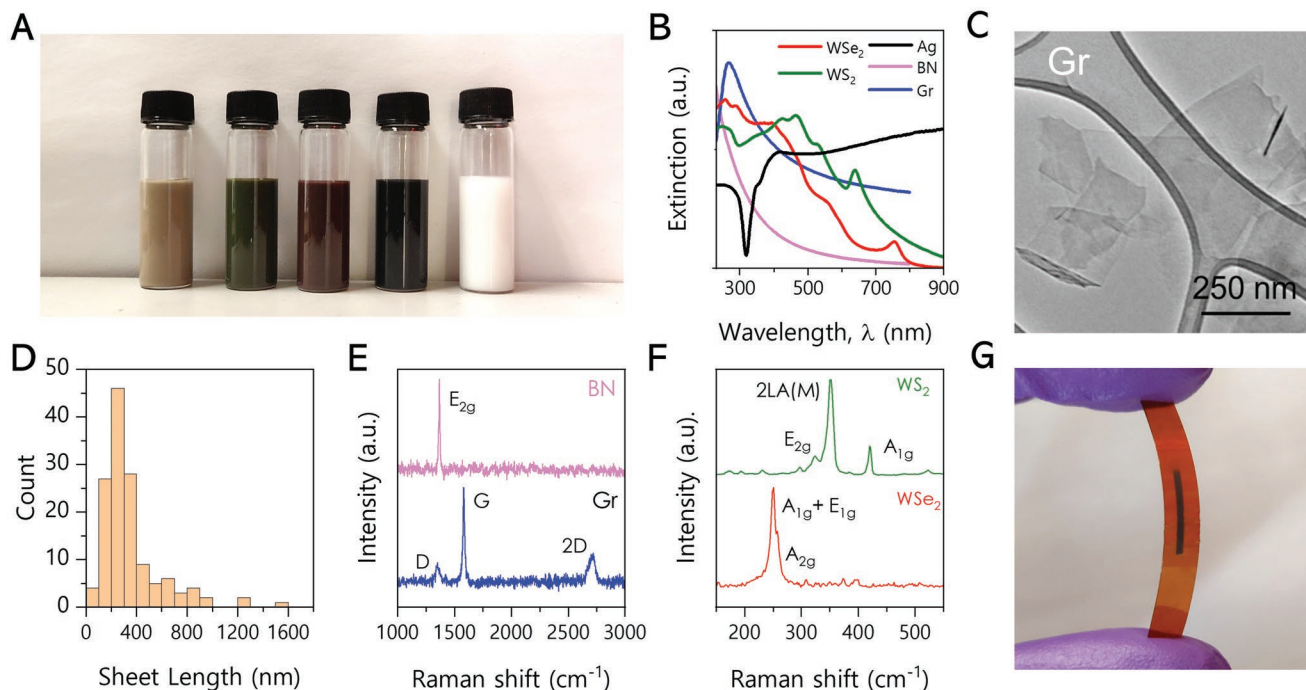
Figure 1. Nanosheet characterisation A) Image of nanosheet dispersions: Ag, WS$_2$, WSe$_2$, Gr, BN. B) UV–vis extinction spectra of all nanosheet dispersions. C) Typical TEM image of Gr nanosheets. Raman spectra measured on networks of D) BN, Gr and E) WS$_2$, WSe$_2$. F) Histogram of graphene nanosheets with average length, <L> = 348 nm. G) Image of a spray coated 2D:2D nanocomposite network.

the filler is usually the more conductive component. Here, the filler is usually graphene, but in one case, it is AgNS. We label the filler volume fraction as ϕ although in specific cases, we will use ϕ_{Gr} or ϕ_{Ag}. In polymer-based nanocomposites, the filler is embedded in a continuous matrix. However, nano:nano composites consist of a mixture of filler particles, matrix particles, and pores, with no continuous phase. In general, spray-coated nanosheets networks are inherently

porous systems, with porosities, ϕ_p, typically between 40% and 60%.[52] Then defining ϕ as the volume of filler particles divided by the total film volume and taking the porosity into account, ϕ can be related to M_f via:[37]

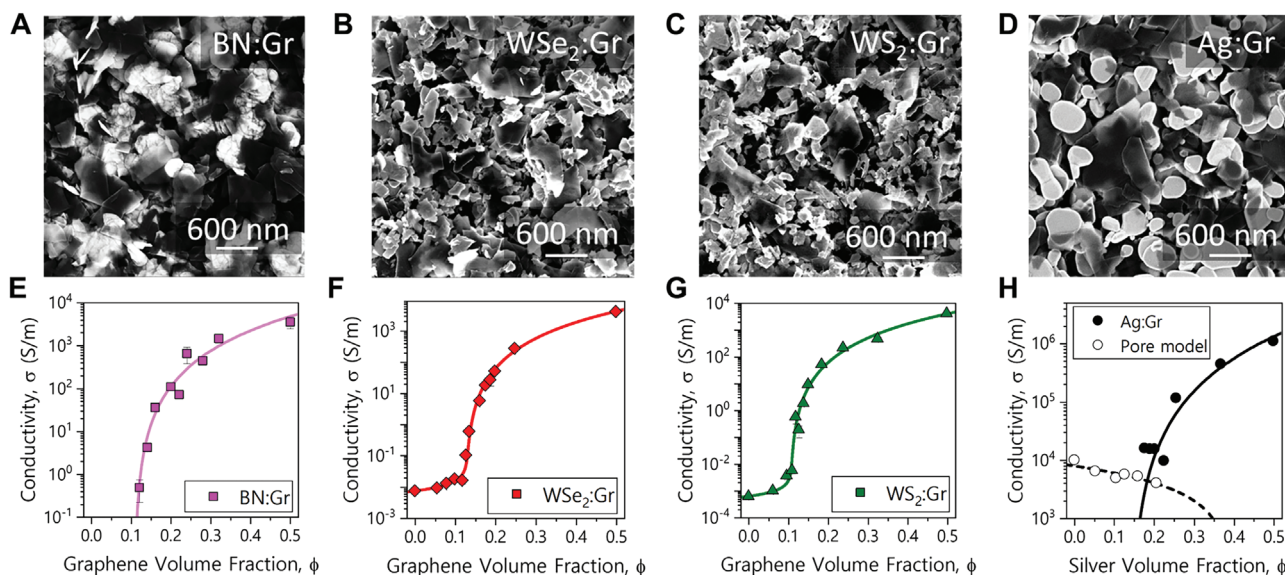$$\phi = \frac{1-\phi_p}{1+\dfrac{\rho_f}{\rho_m}\dfrac{(1-M_f)}{M_f}} \tag{1}$$

Figure 2. 2D:2D nanocomposite characterisation A–D) Representative SEM of nanocomposite networks A) BN:Gr, B) WSe$_2$:Gr, C) WS$_2$:Gr, D) Ag:Gr. E-H) Nanocomposite conductivity, σ plotted as a function of filler volume fraction, ϕ, the solid and dashed lines are fits to various models discussed in the text, fit parameters can be found in Table 1.

Table 1. Fitting parameters obtained from fitting σ versus ϕ data in Figure 2E–H.

	Log[σ_i]	Log[σ_c]	s	t	ϕ_c	Model
BN:Gr	–	4.6± 0.4	–	2.6 ± 0.5	0.109 ± 0.001	Equation 2
WSe$_2$:Gr	−2.15 ± 0.02	4.6 ± 0.1	0.5 ± 0.1	2.6 ± 0.2	0.13 ± 0.01	Equation 4
WS$_2$:Gr	−3.22 ± 0.04	4.7 ± 0.2	0.6 ± 0.3	3.0 ± 0.3	0.10 ± 0.01	Equation 4
Gr:Ag	–	7.1 ± 0.4	–	2.5 ± 0.4	0.160 ± 0.001	Equation 4
Gr:Ag (Pore Model)	–	4.2 ± 0.1	–	0.9 ± 0.3	0.39*	Equation 5

*Fixed value

where ρ_f and ρ_m are densities of the filler and matrix particles. Because the higher conductivity material is considered the filler, we denote graphene as the filler in all cases except the Ag:Gr composites where Ag is the filler. To convert M_f to ϕ, we take: ρ_{Gr}= 2200, ρ_{BN}= 2100, ρ_{WS_2}= 7500, ρ_{WSe_2}= 9300, ρ_{Ag}= 10500 kg m^{-3} and in all cases assume ϕ_p= 0.5.

2.3. Percolative Conductivity

We measured the in-plane DC conductivity of each composite type as a function of filler volume fraction (i.e., ϕ_{Gr} or ϕ_{Ag}) as shown in Figure 2E–H. The effect of introducing a conductive filler into a less conductive matrix on composite conductivity has attracted interest for decades and is by now well understood within the framework of percolation theory.[53] As the filler loading (ϕ) is increased, the conductivity first increases slowly, but as a critical volume fraction, the percolation threshold (ϕ_c) is reached. A sharp increase in conductivity is observed as the first continuous paths of the filler are established. As progressively more filler is added, the conductivity continues to increase steadily toward an ultimate value.[53]

Theoretically, such percolative behavior is generally divided into three separate regimes. Most well-studied is the region above the percolation threshold ($\phi > \phi_c$) wherein the conductivity is described by the percolation equation:

$$\sigma = \sigma_c \left(\frac{\phi - \phi_c}{1 - \phi_c} \right)^t \tag{2}$$

Here, σ_c is a proportionality constant associated with the properties of the filler and t is a percolation exponent.

Equation 2 is applicable when considering systems where the matrix is insulating or does not contribute to conduction, for example, a polymer and conductive filler. This equation should be applicable to our BN:Gr nanocomposites, where BN is the insulating matrix and graphene is the conductive filler (Figure 2E). The variation of conductivity in BN:Gr nanocomposites with increasing graphene loading is consistent with percolation type behavior, with a sharp transition from an insulating to a conducting network at $\phi = 0.12$. The conductivity subsequently increased strongly with ϕ_{Gr}, reaching a value of 4000 S m^{-1} for the all-graphene network (i.e., that with $\phi_{Gr} = 0.5$ due to the presence of pores), which is consistent with previously reported values of LPE graphene.[54,55]

By fitting the conductivity data to Equation 2, the percolative parameters of the network can be extracted (fit parameters

are available in **Table 1**). Here, we find a percolation exponent, $t = 2.6$, which is reasonably close to the predicted universal value of 2 and agrees well with a report on BN:Graphite powder composites.[53,56] Values of t slightly larger than 2 are commonly associated with a broadening of the distribution of junction resistances between the filler particles.[56,57] The percolation threshold obtained for our BN:Gr nanocomposites, $\phi_c = 0.11$ is in the range of previous reports.[51,58]

The analysis above follows the most commonly used procedure where conductivity data only exist above the percolation threshold. The data for WSe$_2$:Gr and WS$_2$:Gr composites in Figure 2F,G show a percolation threshold and region of increasing conductivity for $\phi > \phi_c$. However, the data also show non-zero conductivities for pristine networks of WSe$_2$ (7×10^{-3} S m^{-1}) and WS$_2$ (4×10^{-4} S m^{-1}) as well as for composites at low filler loadings. Thus, analysis will require models beyond Equation 2.

Data for conductivity below the percolation threshold ($\phi < \phi_c$) is seldom reported and rarely fitted. In this regime, there are no continuous filler paths present and instead filler particles exist as islands or clusters within the matrix. In these composites, it is expected that the conductivity is dominated by the paths of least resistance where conductive paths contain segments that traverse both filler and matrix. Thus, such behavior can be observed in composites where the conductivity of the pristine matrix ($\phi = 0$) is non-zero[59] and leads to the following equation:

$$\sigma = \sigma_i \left(\frac{\phi_c - \phi}{\phi_c} \right)^{-s} \tag{3}$$

Here, σ_i is a proportionality constant that can be thought of as the conductivity of a matrix-only film and s is a second percolation exponent. While it would be possible to use Equations 2 and 3 to fit different ϕ-ranges in each of Figure 2F,G, this is unsatisfactory as these equations do not agree on the conductivity when $\phi = \phi_c$. This means a third "cross over" region exists when $\phi \cong \phi_c$.[60] To avoid the need to perform multiple fitting over various regimes, McLachlan et al.[61] developed a functional equation that allows the entire percolation region to be fit using a single equation:

$$(1-\phi)\frac{\sigma_i^{1/s} - \sigma^{1/s}}{\sigma_i^{1/s} + A\sigma^{1/s}} + \phi\frac{\sigma_c^{1/t} - \sigma^{1/t}}{\sigma_c^{1/t} + A\sigma^{1/t}} = 0, \; A = (1-\phi_c)/\phi_c \tag{4}$$

Importantly, this equation reduces to Equation 2 as $\sigma_c \rightarrow \infty$ or Equation 3 as $\sigma_i \rightarrow 0$. Practically speaking, the simplest way

to use this equation is to fit data for ϕ as a function of σ, rather than vice versa as would usually occur.

We have used Equation 4 to fit the conductivity versus volume fraction data in Figure 2F,G (Full list of fit parameters can be found in Table 1). The percolation exponents were observed to be $t = 2.6$ and $t = 3.0$ for WSe$_2$:Gr and WS$_2$:Gr nanocomposites; these results are almost identical t-values those are reported for other 2D:2D networks such as MoS$_2$:Gr[51] and WS$_2$:Gr.[58] We additionally find values for the second percolation exponent, $s = 0.5$ and 0.6 for both composite pairs. This value is somewhat lower that the reported universal value of $s = 0.87$.[53] However, it is consistent with values of $s = 0.40$–1.06, found in powder based composites,[56,59] although it should be noted that much larger values of $s = 5.4$ and 7.6 have been previously observed in 2D:2D composites.[51,62] Equation 4 allows the percolation threshold to be extracted for each nanocomposite, finding $\phi_{c,Gr} = 0.13$ and $\phi_{c,Gr} = 0.10$ for WSe$_2$:Gr and WS$_2$:Gr, respectively. These values are in line with the previous value of $\phi_{c,Gr} = 0.11$ for BN:Gr nanocomposites.

The Ag:Gr conductivity data in Figure 2H are qualifiedly different to that in Figure 2E–G in which the conductivity does not increase monotonically with filler volume fraction. There is a region of sharply increasing conductivity ($\phi_{Ag} > 0.2$), where σ increases in a well-defined manner, before reaching 1.1×10^6 S m^{-1} for an all-silver network ($\phi_{Ag} = 0.5$). Such behavior is consistent with normal above-percolation behavior. However, the region below the apparent percolation threshold ($\phi_{c,Ag} < 0.2$) shows a conductivity that falls off with increasing silver volume fraction. Such a fall-off has not been reported to the authors knowledge.

We first analyze the region where $\phi > 0.2$ (filled circles) before turning to the anomalous behavior at lower ϕ. Fitting using Equation 2, yields $t = 2.5$, which is consistent with the other nanocomposite data discussed above. However, in this instance, we find $\phi_{c,Ag} = 0.16$, which is larger than the previously obtained values for BN, WSe$_2$, and WS$_2$ nanocomposites. We attribute this difference to the relatively low aspect ratio of AgNS, $k = \langle L_{NS}/t_{NS} \rangle$, of ≈ 13.5,[40] compared to graphene which has a much higher ratio $k \approx 150$ (see Supporting Information for details). Previous work shows the percolation threshold depends on the geometry of the filler particles.[63] In fact, in the case of disk like ellipsoids, ϕ_c can vary with the aspect ratio, where large aspect ratios lead to lower values of ϕ_c, as is seen here.[63]

We attribute the anomalous behavior for $\phi_{Ag} < 0.2$ to the effect of poor interparticle charge transfer between graphene nanosheets and silver nanosheets (possibly arising from large junction resistances between the two particles). This means that below the $\phi_{c,Ag}$, where the first all-AgNS conductive path forms, the AgNS do not contribute to conduction at all. However, the AgNS do take up space, reducing the volume of the network of graphene nanosheets which can conduct electricity and essentially act as additional pores. Although the reason for large junction resistances between the AgNs and graphene remain unclear at present, this behavior can be described within the bounds of percolation theory. We introduce a separate percolation model to describe the conductivity of the graphene network (below the silver percolation threshold) in terms of graphene volume fraction. We will now use the fact the total film volume

comprises of graphene, silver, and pores such that $1 = \phi_{Gr} + \phi_{Ag} + \phi_p$. As hypothesized above, when $\phi_{Ag} < 0.2$, the silver does not contribute to conduction due to charge transfer limitations. In this range, conductivity increases with increasing ϕ_{Gr} and so decreases with increasing ϕ_{Ag}. We then apply Equation 2 but writing the graphene volume fraction in terms of the silver volume fraction: $\phi_{Gr} = 1 - \phi_{Ag} - \phi_p$. We assume a nominal percolation threshold, which we term $\phi_{c_p,Gr}$ (which can be related to a nominal silver volume fraction $\phi_{c_p,Ag}$) above which there is so much non-conducting silver and pores that a conducting graphene network does not exist: $\phi_{c_p,Gr} = 1 - \phi_p - \phi_{c_p,Ag}$. Therefore, below the percolation threshold we can write:

$$\sigma = \sigma_c \left(\frac{\phi_{c_p,Ag} - \phi_{Ag}}{\phi_{c_p,Ag} + \phi_p} \right)^{t_p} \tag{5}$$

It is important to note that $\phi_{c_p,Ag}$ is a nominal value which is different from the percolation threshold associated with the formation of a percolating network of AgNS described above. Here, t is re-written as t_p to demonstrate that the exponent is distinct to that in Equation 2.

To facilitate fitting, we estimate a value for $\phi_{c_p,Ag}$, by assuming $\phi_{c_p,Gr} \approx 0.11$, similar to the percolation threshold obtained for BN:Gr, as it is a similar network where BN does not contribute to conduction ($\phi_{c,Gr} \approx 0.11$). Approximating $\phi_p \approx 0.5$ gives $\phi_{c_p,Ag} = 0.39$. Fitting the data then yields $t_p = 0.9$, this is notably smaller than the values for t observed earlier in this work. However, previous work by Barwich et al. suggests the percolation exponent in porosity dependent conductivity of graphene nanosheet films is ≈ 1,[64] which is similar to the value for the "pore effect" found here.

2.4. Piezoresistive Properties of Nano:Nano Composites

Having established that conductivity of these composites is completely described by percolation theory, we now aim to investigate whether the piezoresistive response is also described by percolation theory. The piezoresistive response of each composite film was characterized at low strain by measuring the relative resistance change $\Delta R/R_0$ as a function of applied strain up to $\varepsilon = 1\%$ (**Figure 3**A–D). The gauge factor, G, is defined by $\Delta R/R_0 = G\varepsilon$ and can be extracted from the low-strain slope of these curves. For all composite types, the gauge factor is highly dependent on the filer loading. We have also investigated the cyclic properties of our composite networks; a typical response is shown in Figure S4 (Supporting Information). The films display a stable cyclic response when strained in a sinusoidal manner between 0.2% and 1% strain. The resistance tracks the applied strain well across 250 cycles, with only minimal changes in peak-to-peak values.

The average gauge factor was then plotted as a function of filler volume fraction as shown in Figure 3E–H. In each case, well-defined trends are observed. For all four composite types, the gauge factor increases as the filler volume fraction is decreased from $\phi = 0.5$, increasing rapidly as ϕ is reduced toward the percolation threshold. Similar behavior has previously been observed for polymer nanocomposites, where G diverges as ϕ_c is approached from above.[12]
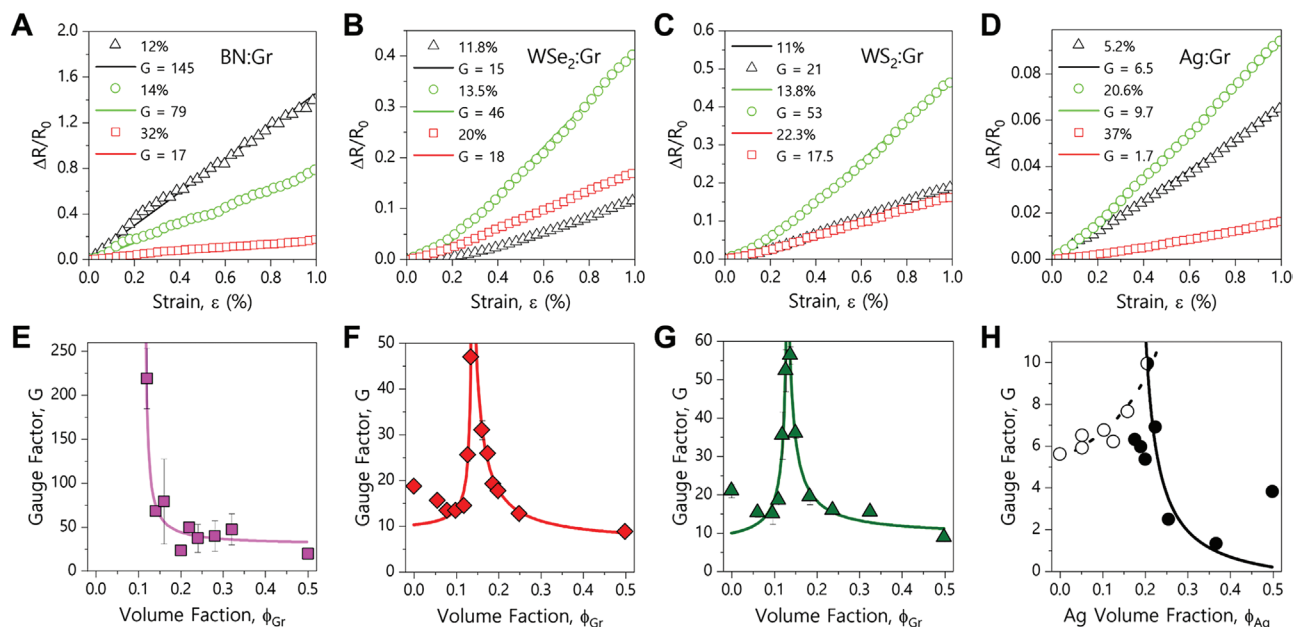
Figure 3. A–D) Fractional resistance change plotted as a function of applied strain to the nanocomposite network, each plot is a representative curve which demonstrates the change in piezoresistive behavior in response to a variation in filler loading. A) BN:Gr, B) WSe₂:Gr, C) WS₂:Gr, D) Ag:Gr. E–H) Gauge factor plotted as a function volume fraction for each nanocomposite pair. The solid and dashed lines are fits to various models discussed in the text, fit parameters can be found in Table 2.

In the case of the Gr:BN composites, no gauge factor data exist below the percolation threshold due to the unmeasurably low conductivities of these composites. This means that, like polymer nanocomposites, only the behavior described above is observed. However, for the WS₂:Gr, WSe₂:Gr, and Ag:Gr composites, non-zero conductivities exist below the percolation threshold. For these composites, as the filler volume fraction reaches the percolation threshold, the gauge factor peaks and then falls off very sharply as ϕ is reduced further. We believe this phenomenon has not been observed previously and is a feature of composites with non-insulating matrices. This data imply that the maximum possible gauge factor exists at the percolation threshold. The maximum observed values of G were 220, 58, 46, and 10 for BN:Gr and WSe₂:Gr WS₂:Gr and Ag:Gr composites, implying that large values of G are obtained when lower conductivity matrices are used.

We note that pristine WSe₂, WS₂, and Ag networks show slightly higher gauge factors than their respective nanocomposites at the lowest loadings of graphene, the reason for this is unclear but we speculate this is due to subtle morphological changes in the composite on addition of filler to the pristine network.

2.5. Modeling 2D:2D Nanocomposite Piezoresistance

We believe that the unusual properties observed in Figure 3E–H are related to the network conductivity and can be explained via percolation theory. Here, we will derive simple models to describe the dependence of gauge factor on filler volume fraction.

In the limit of low strain, it can be shown that,[65]

$$G \approx (1+2\nu) - \frac{1}{\sigma_0}\left(\frac{d\sigma}{d\varepsilon}\right)_0 = (1+2\nu) - \left(\frac{d\ln\sigma}{d\varepsilon}\right)_0 \quad (6)$$

where ν is the Poisson ratio and the subscript zero defines that the quantity should be taken in the limit of low strain. This demonstrates that upon straining a material, the resistance changes for two reasons. First, there is a small change due the effect of strain on sample dimensions, for an incompressible material ($\nu = 0.5$) the contribution to the gauge factor is ≈ 2. Second, there are resistance variations due to changes in material conductivity, this effect is often quite large and can be both positive[66–69] and negative.[13,65]

Previous reports have shown that Equation 6 can be used to obtain an equation for the gauge factor in polymer nanocomposites.[12] We achieve this in a relatively simple manner, by substituting Equation 2 into Equation 6 to yield Equation 7 (details in Supporting Information):

$$G = G_{t,0} + \frac{t}{\phi-\phi_c}\left(\frac{d\phi_c}{d\varepsilon}\right)_0 \quad (7)$$

where $G_{t,0}$ is a composite constant related to other percolation parameters (see Supporting Information) and $(d\phi_c/d\varepsilon)_0$ is the percolation threshold strain dependence (the subscript t on the former quantity is to indicate that this equation is related to Equation 2). We have used this model to fit the data in Figure 3E–H in the region above the electrical percolation threshold, finding it to fit the data well (the fit parameters are listed in **Table 2**). Fitting shows that $G_{t,0}$ takes values between −1 and 28.9, with the lowest value $G_{t,0}$ being associated with

Table 2. Fitting parameters obtained from fitting G versus ϕ data in Figure 3E–H.

	$G_{x,0}$	$[d\phi_c/d\varepsilon]_0$	ϕ_c	Model
BN:Gr	28.9 ± 5.6	0.50 ± 0.08	0.113 ± 0.001	Equation 7
WSe$_2$:Gr (Above ϕ_c)	6.1 ± 1.0	0.32 ± 0.02	0.128 ± 0.001	Equation 7
WSe$_2$:Gr (Below ϕ_c)	8.8 ± 1.4	0.28 ± 0.04	0.139 ± 0.001	Equation 8
WS$_2$:Gr (Above ϕ_c)	9.1 ± 1.1	0.24 ± 0.02	0.123 ± 0.001	Equation 7
WS$_2$:Gr (Below ϕ_c)	6.7 ± 3.2	0.68 ± 0.09	0.136 ± 0.001	Equation 8
Gr:Ag	-1 ± 1	0.15 ± 0.02	0.172 ± 0.001	Equation 7
Gr:Ag (Pore Model)	1.8 ± 0.9	1.6 ± 0.4	$0.390*$	Equation 9

x can take the subscript t, s, or p depending on the model type

the Ag:Gr nanocomposite while the largest value is associated with the BN:Gr nanocomposite. Fitting the data also yields a value for $t(d\phi_c/d\varepsilon)_0$; however, since t is already known from fitting ϕ versus σ, $(d\phi_c/d\varepsilon)_0$ can be extracted for each composite. $(d\phi_c/d\varepsilon)_0$ can be understood intuitively by considering a composite at the percolation threshold so that there is a single connected path of nanosheets through which current can pass. Applying tensile strain to such a system is unlikely to result in new paths forming, instead it is much more likely that the current path will break and lead to an increase in the percolation threshold. Thus, we expect $(d\phi_c/d\varepsilon)_0$ to be positive. Indeed, we find $(d\phi_c/d\varepsilon)_0$ to be positive in all cases, with values ranging between $0.15 \leq (d\phi_c/d\varepsilon)_0 \leq 0.68$. In polymer nanocomposites $(d\phi_c/d\varepsilon)_0$ can vary by several orders of magnitude, for example, Zhang et al. have reported $(d\phi_c/d\varepsilon)_0 = 0.004$ in polyurethane–nanotube composites, while our more recent study suggests $(d\phi_c/d\varepsilon)_0$ can be as large as 3.[12] Additionally, Equation 7 gives us an alternative method for determining ϕ_c, which can be compared to the ϕ_c values obtained from Equation 2, finding relatively good agreement in all cases.

We believe the method of combing Equation 6 with an equation for network conductivity is a very useful one which can be used in various circumstances. For example, in standard composites, we can apply this method to the volume fraction range below the percolation by combining Equations 3 and 6 to yield:

$$G = G_{s,0} + \frac{s}{\phi_c - \phi}\left(\frac{d\phi_c}{d\varepsilon}\right)_0 \tag{8}$$

where $G_{s,0}$ is a composite constant related to other percolation parameters (see Supporting Information), the subscript s is to indicate that this equation is related to Equation 3. Note that this is equation is very similar to Equation 7 with one important difference being that the denominator in Equation 8 is $(\phi_c - \phi)$ rather than $(\phi - \phi_c)$. This means that Equation 8 predicts an increase in G with increasing ϕ (for $\phi < \phi_c$), exactly what is found in the experimental data. This means that, nanocomposites with a measurable conductivity below ϕ_c display a peak in gauge factor centered roughly at the percolation threshold.

The model is used to fit the data for WSe$_2$:Gr and WS$_2$:Gr composites in Figure 3F,G, finding good agreement (the fit parameters are listed in Table 2). We obtain $G_{s,0} = 8.8$ and 6.7 while $(d\phi_c/d\varepsilon)_0 = 0.28$ and 0.68 for WSe$_2$:Gr and WS$_2$:Gr respectively. Similar to Equation 7, Equation 8 also yields values

for ϕ_c. Fitting the data to Equation 8 gives slightly higher values of $\phi_{c,Gr} = 0.139$ and 0.136 when compared to values obtained from Equation 7, $\phi_{c,Gr} = 0.128$ and 0.123. However, the values of ϕ_c obtained from fitting σ_0 versus ϕ as well as both forms of G versus ϕ broadly agree, supporting the validity of the models.

Above, we have used Equations 7 and 8 to fit the WSe2:Gr and WG2:Gr G versus ϕ data separately both above and below the percolation threshold. Of course, it would have been preferrable to use Equation 4 combined with Equation 6 to obtain a model which fits the whole percolative range. However, we were not able to achieve this due to the complicated mathematical form of Equation 4.

Equation 8 describes the G versus ϕ data in standard composites where $\phi < \phi_c$. However, this equation cannot be applied to the Ag:Gr composites because these behave in a non-standard way: due to junction resistance issues, the AgNSs act as extra pores, not contributing to conduction below the percolation threshold. However, we can generate an equation for gauge factor in this situation by combining Equations 5 and 6 to give:

$$G = G_{p,0} + \frac{t_p}{\phi_{c_p,Ag} - \phi_{Ag}}\left(\frac{d\phi_{c_p,Ag}}{d\varepsilon}\right)_0 \tag{9}$$

where $G_{p,0}$ is a composite constant related to other percolation parameters (see SI), the subscript p is to indicate that this equation is related to Equation 5. Again, this equation is similar in form to Equations 7 and 8 but, like Equation 8, predicts an increase in G with increasing ϕ_{Ag} (for $\phi_{Ag} < \phi_{c_p,Ag}$), exactly what is found in the experimental data. We have used this model to fit the data (open circles) for Ag:Gr composites in Figure 3H, finding good agreement (the fit parameters are listed in Table 2). Here, we find $G_{p,0} = 1.8$ and $(d\phi_{c_p,Ag}/d\varepsilon)_0 = 1.6$, while $\phi_{c_p,Ag}$ is a fixed value of 0.39 as described earlier when fitting σ versus ϕ for the same system.

It is worth noting that Equations 7, 8, and 9 are all very similar in form. They all imply that G should be maximized by keeping ϕ as close as possible to ϕ_c. In addition, they all depend on the product of the relevant percolation exponent (i.e., t, s, t_p) and the rate of change of percolation threshold with strain $((d\phi_c/d\varepsilon)_0$ or $(d\phi_{c_p,Ag}/d\varepsilon)_0)$. This highlights that these parameters are key to maximizing piezoresistive sensitivity in percolative strain sensors. We note that large values of the exponent are associated with broad distributions of inter-nanosheet junction resistance, a property that might in some way be engineered. We propose

that the rate of change of percolation threshold with strain is linked to the structure and morphology of the nanosheet network. Again, this is something that might in future be engineered, perhaps by controlling the network deposition method.

2.6. Relationship between Gauge Factor and Conductivity

From the discussion above, it is clear that both conductivity and gauge factor are intimately linked to the filler volume fraction of each network. This is demonstrated in **Figure 4**A,B which uses data for WSe$_2$:Gr, to show a peak in gauge factor very close to the conductivity percolation threshold of the nanocomposites. That both G and σ depend on volume fraction implies the presence of a mutual relationship between them. To investigate this, the gauge factor of each nanocomposite pair is plotted as a function of conductivity in Figure 4C–F. Here, we plot individually the multiple G and σ values that were measured and averaged for each volume fraction. Before discussing the experimental data for each composite type, we will derive simple models to describe that data.

We model the G versus σ behavior by re-writing our previous gauge factor models in terms of conductivity rather than volume fraction. We will first consider the situation where the networks are above the percolation threshold. This is the most general scenario and will apply to most composites. To do this, we combine Equation 7 with Equation 2, to yield Equation 10 which expresses the gauge factor in terms of the zero-strain conductivity:

$$G = G_{t,0} + \frac{t}{1-\phi_c}\left(\frac{\sigma}{\sigma_c}\right)^{-1/t}\left(\frac{d\phi_c}{d\varepsilon}\right)_0 \tag{10}$$

Here, $G_{t,0}$ is a constant identical to that in Equation 7. The model predicts that, above the percolation threshold, the gauge factor should increase monotonically with decreasing conductivity, as observed in the data. Furthermore, the model predicts this effect is highly dependent on the percolation exponent t.

Recalling the previously fitted models, it becomes clear that all the components of Equation 10 have already been determined. The parameters σ_c, ϕ_c and t are found from Equation 2, while a second estimate of ϕ_c and the new terms $G_{t,0}$, $(d\phi_c/d\varepsilon)_0$ are found from Equation 7. Thus, the parameter values may be substituted into Equation 10 to generate a predictive model for σ versus G.

Figure 4C shows G versus σ for BN:Gr in the region above the electrical percolation threshold whereby G increases as σ decreases across several orders of magnitude. In addition, we plot our predictive model using Equation 10 (See **Table 3** for parameter values). Notwithstanding the significant degree of scatter, we find that the model captures the overall shape of the BN:Gr very well. This is important as it demonstrates that these models need not only be used for fitting purposes but can instead be used to predict piezoresistive properties of percolative networks once good estimates of the percolation parameters can be obtained.

A similar model can also be obtained for composite systems that display measurable conductivities below the percolation threshold such as WSe$_2$:Gr, and WS$_2$:Gr networks. This can be achieved by simply combining Equation 8 with Equation 3, which yields:

$$G = G_{s,0} + \frac{s}{\phi_c}\left(\frac{\sigma}{\sigma_i}\right)^{1/s}\left(\frac{d\phi_c}{d\varepsilon}\right)_0 \tag{11}$$

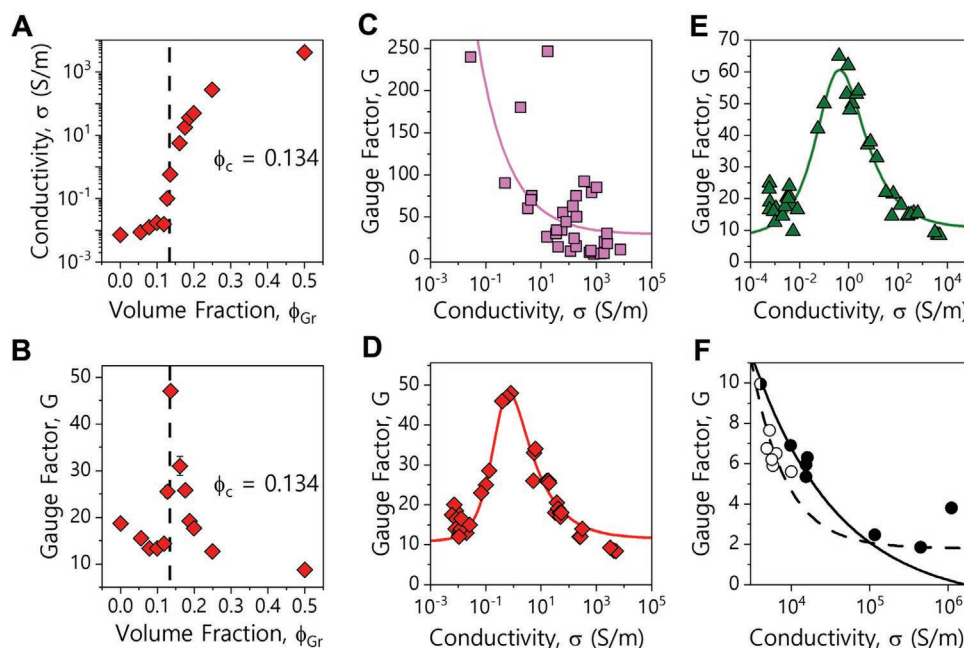**Figure 4.** A) WSe$_2$:Gr conductivity, σ plotted as a function of volume fraction, ϕ. The dashed line shows the relationship between the peak in G and electrical percolation threshold, ϕ_c. B) WSe$_2$:Gr conductivity, G plotted as a function of volume fraction, ϕ. The dashed line shows the relationship between the peak in G and electrical percolation threshold, ϕ_c. C–E) G plotted as a function of nanocomposite conductivity. C) BN:Gr, D) WSe$_2$:Gr, E) WS$_2$:Gr, F) Ag:Gr. The solid and dashed lines are various models discussed in the text, fit parameters can be found in Table 3.

Table 3. Fitting parameters obtained from fitting G versus σ to the data in Figure 4C–F, parameters without errors are fixed values for modelling purposes.

	$G_{x,0}$	Log[σ_i]	s	Log[σ_c]	t	ϕ_c	$[d\phi_c/d\varepsilon]_0$	Model
BN:Gr	28.9	–	–	4.6	2.6	0.11	0.5	Equation 10
WSe$_2$:Gr	11.3 ± 1.5	−2.2	0.95 ± 0.07	4.6	2.2 ± 0.2	0.130	0.14 ± 0.04	Equation 12
WS$_2$:Gr	11.9 ± 0.7	−3.2	1.80 ± 0.3	4.7	1.80 ± 0.3	0.134	0.24 ± 0.08	Equation 12
Gr:Ag	−1	–	–	7.1	2.5	0.16	0.15	Equation 10
Gr:Ag (Pore Model)	1.8	–	–	4.2	0.9	0.39	1.6	Equation 13

x can take the subscript t, σ, or p depending on the model type

where $G_{s,0}$ is constant identical to that in Equation 7.

The WSe$_2$:Gr and WS$_2$:Gr data for σ v G can be divided in two regimes, above and below ϕ_c, and fitted to Equations 10 and 11, respectively. However, as mentioned above, it would be preferable to obtain a model that fits the entire data range (both above and below ϕ_c). Recall that Equation 4 allows conductivity to be described across the whole ϕ-range. By differentiating Equation 4 with respect to strain and combining the result with Equation 6, an equation can be found to fully describe the WSe$_2$:Gr and WS$_2$:Gr datasets (See details in Supporting Information):

$$G = G_{\sigma,0} + \frac{1}{\phi_c^2}\left(\frac{d\phi_c}{d\varepsilon}\right)_0$$

$$\times \frac{\left[\dfrac{1}{\sigma_i^{1/s}/\sigma^{1/s}+A} - \dfrac{1}{\sigma_c^{1/t}/\sigma^{1/t}+A}\right]}{\left[\dfrac{1/t}{\sigma_c^{1/t}/\sigma^{1/t}-1} - \dfrac{1/s}{\sigma_i^{1/s}/\sigma^{1/s}-1} - \dfrac{A/s}{\sigma_i^{1/s}/\sigma^{1/s}+A} + \dfrac{A/t}{\sigma_c^{1/t}/\sigma^{1/t}+A}\right]} \quad (12)$$

where $G_{\sigma,0}$ is an approximate composite constant related to other percolation parameters of both the matrix and filler component of the network (see Supporting Information). This approximation will only be strictly valid when the gauge factor of the both the matrix ($\phi = 0$) and filler ($\phi = 1-\phi_p$) components are approximately equal (i.e., $G_{WSe_2}, G_{WS_2} \approx G_{Gr}$), as is the case here. Importantly in the limiting cases of $\sigma_c \to \infty$ or $\sigma_i \to 0$, Equations 10 and 11 can be recovered from Equation 12. This allows complete fitting of the gauge factor as a function of conductivity for composites with non-zero conductivity both above and below the percolation threshold.

Both the WSe$_2$:Gr and WS$_2$:Gr composites display a peak in gauge factor such that gauge factor begins to decrease as composite conductivity falls below ≈ 1 S m^{-1} (Figure 4D,E). This behavior is contrary to what is observed in our BN:Gr composites (Figure 4C) and indeed all polymer-based nanocomposites. In fact, to the best of our knowledge, this behavior has not been observed previously and is an unexpected result. We had previously hypothesised that a monotonic increase in G with decreasing σ was universal to all composites.[12]

The peak in gauge factor occurs at the electrical percolation threshold for each nanocomposite, is in line with the results of Figure 4A. Ideally, we would model the data using Equation 12 by substitution of parameters as was done for Equation 10, however given the large number of parameters to be substituted, an appropriate prediction was not found. Instead, we have fit the data allowing a comparison of fit parameters to previous models. To facilitate fitting we have fixed some parameters (σ_c, σ_i, ϕ_c) using values obtained from earlier fits, while allowing others to vary ($G_{\sigma,0}$, $(d\phi_c/d\varepsilon)_0$, t, and s). The resultant fit describes the data extremely well, with the peak in gauge factor at $\sigma \approx 1$ S m^{-1} well captured. From the fitting, we obtain $G_{\sigma,0} = 11.3$, 11.9, and $(d\phi_c/d\varepsilon)_0 = 0.14$, 0.24 for WSe$_2$:Gr and WS$_2$:Gr, respectively. The obtained values for t (2.19, 2.36) show excellent agreement with those reported in fits to σ versus ϕ. The s values (0.85,1.80) are somewhat larger than the values found earlier; however overall the same trends are observed with values of t found to be higher than s as is expected from both theory[53] and experiment.[56]

As we have discussed previously, while Equation 11 describes the ϕ versus G data in standard composites where $\phi > \phi_c$, for Ag:Gr composites the variation in conductivity below the percolation threshold is dependent on the fact that AgNSs act as extra pores and do not contribute to conduction. This means a separate equation is required to describe the variation of G with conductivity. We can rewrite Equation 9 in terms of composite conductivity by utilising Equation 5, yielding:

$$G = G_{p,0} + \frac{t_p}{\phi_{c_p,Ag}+\phi_p}\left(\frac{\sigma}{\sigma_c}\right)^{-1/t_p}\left(\frac{d\phi_{c_p,Ag}}{d\varepsilon}\right)_0 \quad (13)$$

where $G_{p,0}$ is identical to that in equation. Similar to Equation 10, Equation 13 can be used as a predictive model. In this instance σ_c, $\phi_{c_p,Ag}$, and t_p can be obtained from fitting Equation 5, while a second estimate of $\phi_{c_p,Ag}$ and the new terms $G_{p,0}$, $(d\phi_c/d\varepsilon)_0$ can be obtained from fitting Equation 9. As before the data contain two regions. Despite the differing percolative mechanisms, the gauge factor increases with decreasing conductivity (Figure 4F), meeting in a shared data point ($G = 10$, $\sigma = 4000$ S m^{-1}). The data in the region above the percolation threshold are denoted by filled circles with the solid line being the predictive model determined from Equation 10. The data below the electrical percolation threshold are denoted by open circles, with the dashed line being the predictive model determined from Equation 13 (See Table 3 for parameter values). We find that the experimental data follow both the predictive models closely in both cases.

In order to frame this work in a wider context we have plotted σ versus G, for a range of bulk and thin film percolative nanocomposites from this work and literature (**Figure 5**).[8,22,70,71] To date researchers have typically considered nanocomposites
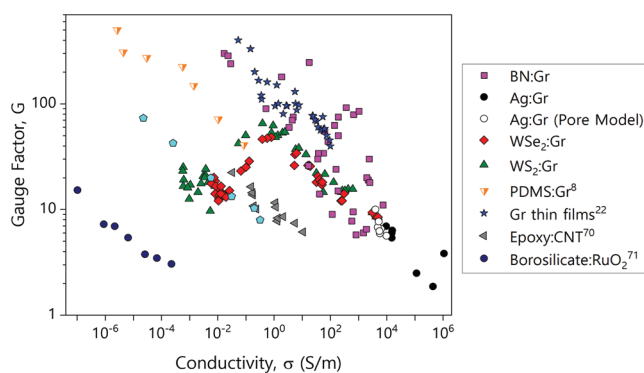
Figure 5. Gauge factor, G plotted as a function of nanocomposite conductivity, σ. The data here include nanocomposite networks from this work as well as materials from literature.[8,22,70,71]

which lie above the percolation threshold, ϕ_c. In such instances the same behavior is nearly always observed, that is, a monotonic increase in G with decreasing conductivity. This behavior is consistent regardless of the type of filler or matrix used, and as indicated above would suggest a universality in the piezoresistive response. Uniquely, we show that it is possible to achieve nanocomposites that have increasing gauge factors with increasing conductivity. In order to achieve such a scenario, we demonstrate that the nanocomposite filler loading must lie in the below ϕ_c regime.

In Figure 5, it is clear that there is a significant spread in the data – some materials perform much better than others. Quantitatively, this can be described by variations in the percolation parameters and their strain-derivatives (e.g., via Equation 10). It is very likely that these parameters depend on a range of properties including those associated with network morphology (porosity, nanosheet, alignment, etc.) and nanosheet dimensions (aspect ratio of both conductor and matrix nanosheets). However, relatively little is known about such factors affect either percolative or piezoresistive factors. Future work will be required to understand such effects. Such an understanding might direct us to controllable factors (such as the dimensions of both nanosheet types) that would allow us to further enhance piezoresistive performance. One factor that we are gaining more control over is nanosheet alignment.[72] However, reports[73,74] suggest that highly aligned nanosheet networks display high electrical conductivities and a relatively small piezoresistive response. This is attributed to a higher degree of areal overlap between the sheets facilitating enhanced charge transport and limiting the effect of strain on the network. Thus, it is likely that more disordered morphologies such as those used here are advantageous. However, more work is required on this topic.

3. Conclusion

In summary, we have studied the electrical and piezoresistive properties of 2D:2D nano:nano composites produced from mixtures of silver, graphene, WSe$_2$, WS$_2$, and BN nanosheets. We have produced various composite types by mixing conducting and insulating down in sheets, conducting

and semiconducting nanosheets, as well as making mixtures of different conducting nanosheets. In all cases, we find the electrical conductivity to scale with filler volume fraction in a manner that is consistent with percolation theory. However, depending on the composite type, we observe different variations of percolation-type behaviors, all of which can be fitted to simple percolation equations. In addition, we have characterized the piezoresistive properties of these networks, measuring the gauge factor as a function of filler loading for each composite type. As with the conductivity, we have found different dependence is of gate factor on filler volume fraction for each composite type. In all cases, we have used percolation theory to develop simple models to describe the piezoresistive behavior with the results and equations facing the data extremely well in each case.

An important outcome of this work is the observation that gauge factor does not always scale monotonically with filler volume fraction or composite conductivity as was previously thought. In fact, for composites fabricated using matrices with nonzero conductivity. Even though the conductivity scales monotonically with both filler volume fraction and composite conductivity, the gauge factor displays a peak when plotted against either filler value fraction or conductivity. This peak limits the maximum gauge factor obtainable. Alternatively, when composites are produced from mixtures of different types of conducting nanosheet, nonmonotonic conductivity versus filler volume fraction behavior is observed. These composites display a peak when gauge factor is plotted versus filler volume fraction but monotonic behavior when gauge factor is plotted versus conductivity. In all cases, these surprising and unusual results can be explained using percolation theory and all arise from the differences in percolation behavior above and below the percolation threshold. Finally, our analysis shows that for all composite types, the gauge factor depends strongly on both the percolation exponent and the rate of change of percolation threshold with strain. In the future, such behavior may allow researchers to engineer composites to have very high gauge factors.

4. Experimental Section

Materials: Bulk powders were sourced from commercial suppliers. Graphite was obtained from Asbury (Grade 3763). WSe$_2$ and WS$_2$ powders from Alfa Aesar (99.8%). Silver nanoplatelets were purchased from Tokusen USA (N300 Nanoflake). BN (>98.5%), Sodium Cholate Hydrate (NaC) (>99%), Isopropanol (IPA) (HPLC grade) were purchased from Sigma–Aldrich. De-Ionised (DI) water (18 MΩ) was produced in house. Substrates used were alumina-coated PET (NM-TP-3GU100 A4) from Mitsubishi Paper Mills in the case of water-based inks and polyimide (DuPont Kapton HN, 125 µm) for IPA based inks.

Layered Crystal Exfoliation: All nanosheet dispersions were prepared in the same way. First, powders (30 mg mL^{-1}) were immersed in 80 mL DI water and NaC (6 mg mL^{-1}). The dispersion was probe sonicated using a Sonics Vibra-Cell VCX-750 ultrasonic processor at 50% amplitude and 6:2 on:off ratio for 1 h. The process was maintained at 7° C to prevent overheating and minimize solvent evaporation. The resulting dispersion was centrifuged (Hettich Mikro 220R centrifuge) for 1 h at 3824 g, the supernatant was discarded, and the sediment was redispersed in 80 mL DI water and NaC (2 mg mL^{-1}) via bath sonication. The dispersions were then sonicated for 8 h at 50% amplitude and 4:4 on:off ratio. Unexfoliated and large nanosheets were removed by centrifuging the dispersions

at 106 g for 2 h and discarding the sediment. The supernatant was then centrifuged at 3824 g for 2 h, discarding the supernatant and redispersing the sediment in 80 mL DI water and NaC (2 mg mL^{-1}) to obtain stock dispersions of nanosheet ink. The nanosheet concentration was determined via vacuum filtration of a fixed dispersion volume onto an alumina membrane and measuring the change in mass.

Water-Based Nanocomposite Inks: To remove excess NaC, the graphene stock dispersion was centrifuged at 3824 g for 2 h, supernatant discarded, and sediment redispersed in DI waster. AgNS were delivered as a viscous paste. Upon dilution with DI water workable inks could be obtained. Ink concentration was determined via vacuum filtration of a fixed ink volume onto an alumina membrane and measuring the change in mass. Composite inks of different concentrations were achieved by mixing AgNS and graphene inks in various ratios. The ink concentration was tailored so that the solids volume content was the same in all inks. In this case, the starting AgNS ink had a concentration of 2 mg mL^{-1} and graphene ink had a concentration of 0.43 mg mL^{-1}. This means the volume of composite ink was equal in all cases regardless of the AgNS loading.

IPA-Based Nanocomposite Inks: Transfer of stock dispersions to IPA was achieved by centrifuging at 3824 g for 2 h. The sediment was then redispersed in IPA. This was repeated three times to remove a residual water or surfactant. Nanocomposite inks were then achieved by the same methods as those described above.

UV–Vis Spectroscopy: Extinction spectra were recorded using a Varian Cary 50 UV–vis spectrophotometer in 0.5 nm increments with a 10 mm quartz cuvette.

Spray Coating: Nanocomposite inks were spray-coated using a Harder and Steenbeck Infinity Airbrush, in tandem with a Janome JR23000N mobile gantry. A platen was used to heat the substrates to 70 °C. A N$_2$ back pressure of 4 psi, nozzle diameter of 400 μm, and stand-off distance of 10 cm were also used. Single line patterns of 15 mm × 1 mm were achieved by spray-coating through a patterned steel mask onto polyimide substrates (35 mm × 5 mm)

Profilometry: A Bruker Detak Profilometer was used to obtain thin film thickness with a stylus tip of 12.5 μm and stylus force of 9.8 μN. Film thickness was measured on films sprayed on glass substrates and were found to be between 600 and 1000 nm thick.

Electrical and Electromechanical Measurements: Resistance measurements were carried out using a Keithley KE2601 source meter in a 2-probe mode, controlled by LabView software. Electromechanical tests were carried out in conjunction with a Zwick Z0.5 ProLine Tensile Tester (100 N Load Cell). All samples had a gauge length, $L_0 = 25$ mm. Tensile measurements were carried out at a strain rate of 1% s^{-1}.

Raman Spectroscopy: Raman spectra were acquired with Horiba Jobin Yvon set up using a laser line of 532 nm. A 10X objective was used with a neutral density filter to avoid heating of sample. The samples for the Raman measurements were prepared by drop casting the dispersion (≈0.5 mg mL^{-1}) onto the heated silicon wafer coated with 300 nm of silicon dioxide.

SEM: SEM images of 2D:2D nanocomposite thin films were captured using a Zeiss Ultra scanning electron microscope with accelerating voltages of 2–5 kV.

TEM: A JEOL JEM-2100 LaB6 transmission electron microscope operating at 200 kV was used to provide images of individual nanosheets. The dispersion was diluted to low concentrations and drop-cast onto an ultrathin carbon film TEM grid provided by Ted Pella, Inc. The TEM grid was placed on a piece of filter paper in order to wick away any excess solvent and then dried overnight in a vacuum oven. The images were used to obtain a statistical analysis of the nanosheet lengths, defined as the longest axis of each nanosheet.

Supporting Information

Supporting Information is available from the Wiley Online Library or from the author.

Conflict of Interest

The authors declare no conflict of interest.

Data Availability Statement

The data that support the findings of this study are available from the corresponding author upon reasonable request.

[1] T. R. Ray, J. Choi, A. J. Bandodkar, S. Krishnan, P. Gutruf, L. Tian, R. Ghaffari, J. A. Rogers, *Chem. Rev.* **2019**, *119*, 5461.

[2] P. Won, K. K. Kim, H. Kim, J. J. Park, I. Ha, J. Shin, J. Jung, H. Cho, J. Kwon, H. Lee, S. H. Ko, *Adv. Mater.* **2021**, *33*, 2002397.

[3] A. Bolotsky, D. Butler, C. Dong, K. Gerace, N. R. Glavin, C. Muratore, J. A. Robinson, A. Ebrahimi, *ACS Nano* **2019**, *13*, 9781.

[4] Y. Pang, Z. Yang, Y. Yang, T.-L. Ren, *Small* **2020**, *16*, 1901124.

[5] A. G. Kelly, D. O'Suilleabhain, C. Gabbett, J. N. Coleman, *Nat. Rev. Mater.* **2021**, *7*, 217.

[6] A. L. Window, in *Strain Gauge Technology*, Springer, Berlin, Germany **1992**.

[7] D. P. O'Driscoll, S. McMahon, J. Garcia, S. Biccai, A. G. Kelly, S. Barwich, M. Moebius, C. S. Boland, J. N. Coleman, *Small* **2020**, *17*, 2006542.

[8] C. S. Boland, U. Khan, G. Ryan, S. Barwich, R. Charifou, A. Harvey, C. Backes, Z. Li, M. S. Ferreira, M. E. Möbius, R. J. Young, J. N. Coleman, *Science* **2016**, *354*, 1257.

[9] Q. Zheng, J.-H. Lee, X. Shen, X. Chen, J.-K. Kim, *Mater. Today* **2020**, *36*, 158.

[10] C. S. Boland, *ACS Nano* **2019**, *13*, 13627.

[11] M. Amjadi, K.-U. Kyung, I. Park, M. Sitti, *Adv. Funct. Mater.* **2016**, *26*, 1678.

[12] J. R. Garcia, D. O'Suilleabhain, H. Kaur, J. N. Coleman, *ACS Appl. Nano Mater.* **2021**, *4*, 2876.

[13] S. Biccai, C. S. Boland, D. P. O'Driscoll, A. Harvey, C. Gabbett, D. R. O'Suilleabhain, A. J. Griffin, Z. Li, R. J. Young, J. N. Coleman, *ACS Nano* **2019**, *13*, 6845.

[14] R. Razavi, Y. Zare, K. Y. Rhee, *Polym. Compos.* **2019**, *40*, 801.

[15] A. J. Marsden, D. G. Papageorgiou, C. Vallés, A. Liscio, V. Palermo, M. A. Bissett, R. J. Young, I. A. Kinloch, *2D Mater.* **2018**, *5*, 032003.

**ADVANCED
SCIENCE NEWS**

www.advancedsciencenews.com

**ADVANCED
FUNCTIONAL
MATERIALS**

www.afm-journal.de

[16] R. J. Young, M. Liu, I. A. Kinloch, S. Li, X. Zhao, C. Vallés, D. G. Papageorgiou, *Compos. Sci. Technol.* **2018**, *154*, 110.

[17] D. S. A. De Focatiis, D. Hull, A. Sánchez-Valencia, *Plast., Rubber Compos.* **2012**, *41*, 301.

[18] J.-S. Kim, G.-W. Kim, *Sensors* **2017**, *17*, 229.

[19] H. Liu, Y. Li, K. Dai, G. Zheng, C. Liu, C. Shen, X. Yan, J. Guo, Z. Guo, *J. Mater. Chem.* **2016**, *4*, 157.

[20] F. Zhang, H. Hu, S. Hu, J. Yue, *J. Adv. Ceram.* **2021**, *10*, 1350.

[21] M. Hempel, D. Nezich, J. Kong, M. Hofmann, *Nano Lett.* **2012**, *12*, 5714.

[22] E. Caffrey, J. R. Garcia, D. O'Suilleabhain, C. Gabbett, T. Carey, J. N. Coleman, *ACS Appl. Mater. Interfaces* **2022**, *14*, 7141.

[23] S. Ryu, P. Lee, J. B. Chou, R. Xu, R. Zhao, A. J. Hart, S.-G. Kim, *ACS Nano* **2015**, *9*, 5929.

[24] X. Li, R. Zhang, W. Yu, K. Wang, J. Wei, D. Wu, A. Cao, Z. Li, Y. Cheng, Q. Zheng, R. S. Ruoff, H. Zhu, *Sci. Rep.* **2012**, *2*, 870.

[25] Y. Cai, J. Shen, Z. Dai, X. Zang, Q. Dong, G. Guan, L.-J. Li, W. Huang, X. Dong, *Adv. Mater.* **2017**, *29*, 1606411.

[26] Y. Cai, J. Shen, G. Ge, Y. Zhang, W. Jin, W. Huang, J. Shao, J. Yang, X. Dong, *ACS Nano* **2018**, *12*, 56.

[27] J. Shi, X. Li, H. Cheng, Z. Liu, L. Zhao, T. Yang, Z. Dai, Z. Cheng, E. Shi, L. Yang, Z. Zhang, A. Cao, H. Zhu, Y. Fang, *Adv. Funct. Mater.* **2016**, *26*, 2078.

[28] T. D. Gupta, T. Gacoin, A. C. H. Rowe, *Adv. Funct. Mater.* **2014**, *24*, 4522.

[29] G. Hassan, M. U. Khan, J. Bae, A. Shuja, *Sci. Rep.* **2020**, *10*, 18234.

[30] S. Chen, Y. Wei, X. Yuan, Y. Lin, L. Liu, *J. Mater. Chem. C* **2016**, *4*, 4304.

[31] S. Pan, Z. Pei, Z. Jing, J. Song, W. Zhang, Q. Zhang, S. Sang, *RSC Adv.* **2020**, *10*, 11225.

[32] J. Zhao, C. He, R. Yang, Z. Shi, M. Cheng, W. Yang, G. Xie, D. Wang, D. Shi, G. Zhang, *Appl. Phys. Lett.* **2012**, *101*, 063112.

[33] Z. Chen, T. Ming, M. M. Goulamaly, H. Yao, D. Nezich, M. Hempel, M. Hofmann, J. Kong, *Adv. Funct. Mater.* **2016**, *26*, 5061.

[34] K. Takei, Z. Yu, M. Zheng, H. Ota, T. Takahashi, A. Javey, *Proc. Natl. Acad. Sci. USA* **2014**, *111*, 1703.

[35] A. Chhetry, M. Sharifuzzaman, H. Yoon, S. Sharma, X. Xuan, J. Y. Park, *ACS Appl. Mater. Interfaces* **2019**, *11*, 22531.

[36] X. Shi, S. Liu, Y. Sun, J. Liang, Y. Chen, *Adv. Funct. Mater.* **2018**, *28*, 1800850.

[37] C. Gabbett, C. S. Boland, A. Harvey, V. Vega-Mayoral, R. J. Young, J. N. Coleman, *Chem. Mater.* **2018**, *30*, 5245.

[38] C. Backes, T. M. Higgins, A. Kelly, C. Boland, A. Harvey, D. Hanlon, J. N. Coleman, *Chem. Mater.* **2017**, *29*, 243.

[39] N. C. Jonathan, M. Lotya, A. O'Neill, D. B. Shane, J. King Paul, U. Khan, K. Young, A. Gaucher, S. De, J. S. Ronan, V. S. Igor, K. A. Sunil, G. Stanton, H.-Y. Kim, K. Lee, T. K. Gyu, S. D. Georg, T. Hallam, J. B. John, J. W. Jing, F. D. John, C. G. Jaime, G. Moriarty, A. Shmeliov, J. N. Rebecca, M. P. James, M. G. Eleanor, K. Theuwissen, W. McComb David, D. N. Peter, et al., *Science* **2011**, *331*, 568.

[40] A. G. Kelly, J. O'Reilly, C. Gabbett, B. Szydłowska, D. O'Suilleabhain, U. Khan, J. Maughan, T. Carey, S. Sheil, P. Stamenov, J. N. Coleman, *Small* **2022**, *18*, 2105996.

[41] C. Backes, K. R. Paton, D. Hanlon, S. Yuan, M. I. Katsnelson, J. Houston, R. J. Smith, D. McCloskey, J. F. Donegan, J. N. Coleman, *Nanoscale* **2016**, *8*, 4311.

[42] A. Griffin, A. Harvey, B. Cunningham, D. Scullion, T. Tian, C.-J. Shih, M. Gruening, J. F. Donegan, E. J. G. Santos, C. Backes, J. N. Coleman, *Chem. Mater.* **2018**, *30*, 1998.

[43] V. Vega-Mayoral, D. Vella, T. Borzda, M. Prijatelj, I. Tempra, E. A. A. Pogna, S. Dal Conte, P. Topolovsek, N. Vujicic, G. Cerullo, D. Mihailovic, C. Gadermaier, *Nanoscale* **2016**, *8*, 5428.

[44] C. Backes, R. J. Smith, N. McEvoy, N. C. Berner, D. McCloskey, H. C. Nerl, A. O'Neill, P. J. King, T. Higgins, D. Hanlon, N. Scheuschner, J. Maultzsch, L. Houben, G. S. Duesberg, J. F. Donegan, V. Nicolosi, J. N. Coleman, *Nat. Commun.* **2014**, *5*, 4576.

[45] Q. Lu, K.-J. Lee, K.-B. Lee, H.-T. Kim, J. Lee, N. V. Myung, Y.-H. Choa, *J. Colloid Interface Sci.* **2010**, *342*, 8.

[46] B. J. Wiley, Y. Chen, J. M. McLellan, Y. Xiong, Z.-Y. Li, D. Ginger, Y. Xia, *Nano Lett.* **2007**, *7*, 1032.

[47] A. Callegari, D. Tonti, M. Chergui, *Nano Lett.* **2003**, *3*, 1565.

[48] X. M. Sun, Y. D. Li, *Adv. Mater.* **2005**, *17*, 2626.

[49] A. Berkdemir, H. R. Gutiérrez, A. R. Botello-Méndez, N. Perea-López, A. L. Elías, C.-I. Chia, B. Wang, V. H. Crespi, F. López-Urías, J.-C. Charlier, H. Terrones, M. Terrones, *Sci. Rep.* **2013**, *3*, 1755.

[50] A. G. Kelly, V. Vega-Mayoral, J. B. Boland, J. N. Coleman, *2D Mater.* **2019**, *6*, 045036.

[51] G. Cunningham, M. Lotya, N. McEvoy, G. S. Duesberg, P. van der Schoot, J. N. Coleman, *Nanoscale* **2012**, *4*, 6260.

[52] G. Kelly Adam, T. Hallam, C. Backes, A. Harvey, S. Esmaeily Amir, I. Godwin, J. Coelho, V. Nicolosi, J. Lauth, A. Kulkarni, S. Kinge, D. A. Siebbeles Laurens, S. Duesberg Georg, N. Coleman Jonathan, *Science* **2017**, *356*, 69.

[53] D. Stauffer, *Phys. Rep.* **1979**, *54*, 1.

[54] K. Pan, Y. Fan, T. Leng, J. Li, Z. Xin, J. Zhang, L. Hao, J. Gallop, K. S. Novoselov, Z. Hu, *Nat. Commun.* **2018**, *9*, 5197.

[55] S. De, J. N. Coleman, *ACS Nano* **2010**, *4*, 2713.

[56] J. Wu, D. S. McLachlan, *Phys. Rev. B* **1997**, *56*, 1236.

[57] P. M. Kogut, J. P. Straley, *J. Phys. C: Solid State Phys.* **1979**, *12*, 2151.

[58] D. O'Suilleabhain, V. Vega-Mayoral, A. G. Kelly, A. Harvey, J. N. Coleman, *ACS Appl. Mater. Interfaces* **2019**, *11*, 8545.

[59] C. Chiteme, D. S. McLachlan, G. Sauti, *Phys. Rev. B* **2007**, *75*, 094202.

[60] J. P. Straley, *J. Phys. C: Solid State Phys.* **1976**, *9*, 783.

[61] D. S. McLachlan, M. Blaszkiewicz, R. E. Newnham, *J. Am. Ceram. Soc.* **1990**, *73*, 2187.

[62] A. G. Kelly, C. Murphy, V. Vega-Mayoral, A. Harvey, A. S. Esmaeily, T. Hallam, D. McCloskey, J. N. Coleman, *2D Mater.* **2017**, *4*, 041006.

[63] E. J. Garboczi, K. A. Snyder, J. F. Douglas, M. F. Thorpe, *Phys Rev E* **1995**, *52*, 819.

[64] S. Barwich, J. Medeiros De Araújo, A. Rafferty, C. Gomes Da Rocha, M. S. Ferreira, J. N. Coleman, *Carbon* **2021**, *171*, 306.

[65] A. S. Fiorillo, C. D. Critello, S. A. Pullano, *Sens. Actuator A-Phys.* **2018**, *281*, 156.

[66] S. Chen, Y. Song, D. Ding, Z. Ling, F. Xu, *Adv. Funct. Mater.* **2018**, *28*, 1802547.

[67] S. Chun, Y. Choi, W. Park, *Carbon* **2017**, *116*, 753.

[68] C. S. Boland, U. Khan, C. Backes, A. O'Neill, J. McCauley, S. Duane, R. Shanker, Y. Liu, I. Jurewicz, A. B. Dalton, J. N. Coleman, *ACS Nano* **2014**, *8*, 8819.

[69] M. Amjadi, A. Pichitpajongkit, S. Lee, S. Ryu, I. Park, *ACS Nano* **2014**, *8*, 5154.

[70] N. Hu, Y. Karube, M. Arai, T. Watanabe, C. Yan, Y. Li, Y. L. Liu, H. Fukunaga, *Carbon* **2010**, *48*, 680.

[71] P. F. Carcia, A. Suna, W. D. Childers, *J. Appl. Phys.* **1983**, *54*, 6002.

[72] Z. Y. Lin, Y. Liu, U. Halim, M. N. Ding, Y. Y. Liu, Y. L. Wang, C. C. Jia, P. Chen, X. D. Duan, C. Wang, F. Song, M. F. Li, C. Z. Wan, Y. Huang, X. F. Duan, *Nature* **2018**, *562*, 254.

[73] Z. Chen, T. Ming, M. M. Goulamaly, H. M. Yao, D. Nezich, M. Hempel, M. Hofmann, J. Kong, *Adv. Funct. Mater.* **2016**, *26*, 5061.

[74] Z. C. Yan, D. Xu, Z. Y. Lin, P. Q. Wang, B. C. Cao, H. Y. Ren, F. Song, C. Z. Wan, L. Y. Wang, J. X. Zhou, X. Zhao, J. Chen, Y. Huang, X. F. Duan, *Science* **2022**, *375*, 852.

2214855 (12 of 12)